Three-dimensional simple conformal symplectic particle-in-cell methods for simulations of high power microwave devices

Yue Wang [a], Jianguo Wang [a,b,*], Zaigao Chen [a,b], Guoxin Cheng [a], Pan Wang [a]

[a] *Northwest Institute of Nuclear Technology, Xi'an, Shaanxi 710024, China*
[b] *Key Laboratory for Physical Electronics and Devices of the Ministry of Education, Xi'an Jiaotong University, Xi'an 710049, China*

ARTICLE INFO

ABSTRACT

To overcome the staircase error in the traditional particle-in-cell (PIC) method, a three dimensional (3D) simple conformal (SC) symplectic PIC method is presented in this paper. The SC symplectic finite integration technique (FIT) scheme is used to advance the electromagnetic fields without reduction of the time step. Particles are emitted from conformal boundaries with the charge conserving emission scheme and moved by using the relativistic Newton–Lorentz force equation. The symplectic formulas of auxiliary-differential equation, complex frequency shifted perfectly matched layer (ADE-CFS-PML) are given for truncating the open boundaries, numerical results show that the maximum relative error of truncation is less than 90 dB. Based on the surface equivalence theorem, the computing algorithms of conformal signals' injection are given, numerical results show that the algorithms can give the right mode patterns and the errors of cutoff frequencies could be as low as 0.1%. To verify the conformal algorithms, a magnetically insulated line oscillator is simulated, and the results are compared to those provided by using the 2.5D UNIPIC code, which show that they agree well. The results also show that the high order symplectic integration method can suppress the numerical Cherenkov radiation.

© 2016 Elsevier B.V. All rights reserved.

1. Introduction

The particle-in-cell (PIC) method has been widely used in the generation of high-power microwave (HPM) as a means to understand the very complex nonlinear physical process of the beam–wave interaction [1,2], and the PIC codes have revolutionized the HPM research field. In the PIC method, the electromagnetic fields are updated using the second-order, finite-difference time-domain (FDTD) [3] or finite integration technique (FIT) [4,5] method, and the particles are moved using the relativistic Newton–Lorentz force equation. Based on this method, some fully electromagnetic PIC codes have been developed, for example, MAGIC [6], OOPIC (object-oriented PIC) [7], KARAT [8], ICEPIC [9], MAFIA [10], Vorpal [11], UNIPIC [12,13], and so on.

One of the most difficult problems encountered using a PIC code to simulate the HPM devices is the treatment of the curved conducting boundaries and cathode surface, which may exist in some real HPM devices. For the staircased approach, it is easy to generate grids and the algorithm has high efficiency, but the main disadvantage of this approach is that the solution becomes the first-order accuracy due to the first-order approximation to the boundaries, which introduces large discretization errors, even when the grid size is small. Especially, for the particles' emission, the particles are emitted from the staircased surface, the velocity direction of the particle cannot guarantee to be normal to the original boundary of the cathode. Basically, there are two types of methods to accurately model the curved boundaries, namely the unstructured meshes and the structured meshes. For the unstructured meshes, a discontinuous Galerkin (DG) scheme for solving the Maxwell–Vlasov equations in time-domain was developed to model the HPM sources [14]. For the structured meshes, some conformal methods to accurately model the curved surface were studied.

To increase the accuracy of the boundary approximation while preserving many benefits of the original algorithms, the partially filled cells (PFC) [15] or cut-cell (embedded boundary method) approach [16] with the second-order accuracy was developed. Accordingly, some conformal methods for updating the electromagnetic fields were also developed, such as the contour path FDTD (CP-FDTD) scheme [15], enlarged cell technique conformal FDTD (ECT-CFDTD) scheme [17], uniformly stable

* Corresponding author at: Northwest Institute of Nuclear Technology, Xi'an, Shaanxi 710024, China.
 E-mail address: wanguiuc@mail.xjtu.edu.cn (J. Wang).

conformal finite integration technique (USC-FIT) scheme, simple conformal FIT (SC-FIT) scheme [18], CP-WCS FDTD Method [19], etc. In the ECT-CFDTD/USC-FIT scheme, to avoid the reduction of time step compared to the conventional staircase method, the magnetic fluxes from the neighboring cells are interpolated to the small cell, and the enlarged magnetic voltage of the small cell is averaged to the neighboring magnetic voltages. But when this scheme is used in the PIC method, the interpolating and averaging operations may destroy the charge conversation near the cut-cell emission boundary, even using the charge conservation weighting scheme. Unlike the ECT-CFDTD/USC-FIT scheme, the SC-FIT scheme does not use any interpolating and averaging operation, and hence, it will not destroy the charge conservation, meanwhile, the reduction of edge length is introduced to avoid the reduction of time step.

Additionally, the traditional FDTD method used for dealing with the time derivatives in the Maxwell's equations can lead to significant numerical dispersion [20], so the FDTD-PIC algorithm may cause the numerical Cherenkov instability [21,22], which is particularly serious for the relativistic electron beams [23]. The pseudo-spectral analytical time-domain (PSATD) algorithm is free of numerical Cherenkov instability [24]. For the PSATD algorithm, the fields are exact in space and second-order accurate in time, Fourier transforms of fields and currents are required at each time step, so the fields should be evaluated as a set of modes in Fourier space, which is computationally expensive. Unlike the PSATD algorithm, the symplectic integrator (SI) [20] is a high order algorithm to simulate the dynamics of electromagnetic fields in time and second-order accurate in space, it can preserve the dynamical invariants up to a desired order of accuracy, and hence, it can greatly decrease the numerical dispersion. In Ref. [25], a variational multi-symplectic PIC algorithm with smoothing functions for the Vlasov–Maxwell system was introduced and applied to simulate the nonlinear mode conversion from extraordinary waves to Bernstein waves [26], but this algorithm is constructed based on the Lagrangian density for a collection of N nonrelativistic charged particles together with the electromagnetic field, and it does not suit for the simulations of HPM devices involving the relativistic charged beams. So, in this paper, for decreasing the dispersion error and also having the capability to solve the relativistic Newton–Lorentz force equation explicitly, SI method is employed to update the electromagnetic fields, and the relativistic charged particle's movement equation is solved by using the traditional Boris advancing method.

For emission/absorption of the charged particles, when a cut-cell boundary is involved, the challenge is how to deal with the boundary conditions of particles to ensure that Gauss's law is preserved. A macro-particle, which crosses a cut-cell boundary and leaves the simulation region, should be removed. And the macro-particle, which is emitted from a cut-cell boundary, should be injected there. However, immediate removal or injection from a cut-cell boundary can lead to non-zero divergence of the electric field. This can accumulate to an unphysical degree [16]. One may simply forcefully displace a particle to the nearest PEC (perfect electric conductor) node, compute currents as if this was the actual trajectory, and hence insure no remnant charge [16]. But the currents may produce large numerical noise, where the noise can couple to high frequency modes trapped within the cut-cells [16].

In this paper, we present a new SC symplectic PIC method. The SC method is used to overcome the shortcomings of the staircased meshes without reduction of time step, and the symplectic integrator is introduced to reduce the phase error in time. On the other hand, the cut-cell conformal scheme of particle injection is improved for reducing the numerical noise while preserving the charge conservation. For the truncation of open port, the auxiliary-differential equation (ADE) form of the complex
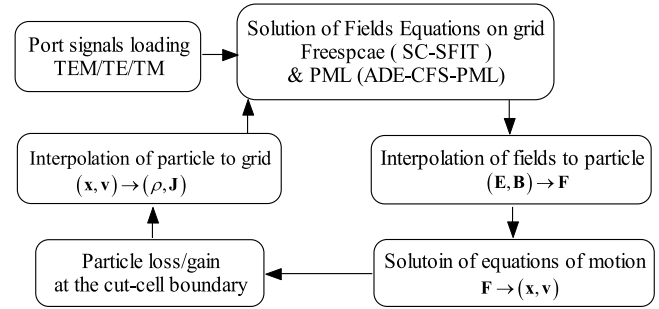

Fig. 1. Flow chart for SC symplectic PIC scheme.

frequency shifted [27] perfectly matched layer (CFS-PML) [28] for symplectic FIT algorithm is introduced first. The conformal port mode loading algorithm is given by solving the discrete eigenvalue equation at the conformal port. Additionally, Friedman damping scheme [29] is employed to suppress the high frequency waves.

2. SC symplectic PIC method

Based on our recent developed model design and conformal grid generation techniques [30], the SC symplectic PIC method is developed to get more accuracy without loss of too much efficiency to simulate the HPM tubes. The general flow of this method is shown in Fig. 1.

The fields are defined at discrete locations in space. Using the SC scheme to maintain the curved boundary values without reduction of the time step, and employing the symplectic integrator, the fields are advanced at discrete times. For the port's mode loading, the elements belonging to the port can be selected first, the distribution modes of fields at the port can be computed and be loaded as the input signals by solving the eigenvalue equations of these elements. For the open port (or output port) boundaries, the ADE-CFS-PML is employed to truncate the outgoing waves. Unlike the convolutional PML (CPML) with the discrete recursive convolution algorithm [31–33], the parameters of ADE-CFS-PML are not the exponential functions of time step, so it is easy to introduce a high-order SI method to maintain the time derivatives.

The particles are defined in the continuum spaces of both position and velocity. In our scheme, Boris advancing method with the time-centered second-order accuracy is used to solve the relativistic Newton–Lorentz force equation. For conformal emission and absorption of particles, the cut-cell method is slightly modified, namely, the particle is absorbed only when it moves into a cell fully filled by PEC. If a particle is in a PFC, it is pushed by the fields normally. So when a particle is emitted with an initial velocity at the nearest exterior node just as the cut-cell emission scheme, not being artificially forced to move to the cut-cell boundary, the particle moves with its own velocity into a PFC or a non-filled cell by PEC.

The electromagnetic fields and particles are coupled through the current term in the Maxwell's equations. In our scheme, ρ and $\boldsymbol{J}$ are computed by the density decomposition method [34], which is a charge conservation scheme.

2.1. The definition of grid elements in conformal grid system

Given a boundary representation (B-rep) of a shape [35], in order to describe the topology of discrete boundaries in the discrete grid system, the relative orientation relationship between line and face on a PFC for PEC geometries should be defined.

Suppose that the direction of a grid line is along one coordinate axis, u_0, u_1, and u_2 are used to define the direction of grid lines, (u_0, u_1, u_2) may be (x, y, z), (y, z, x) or (z, x, y). For convenience,

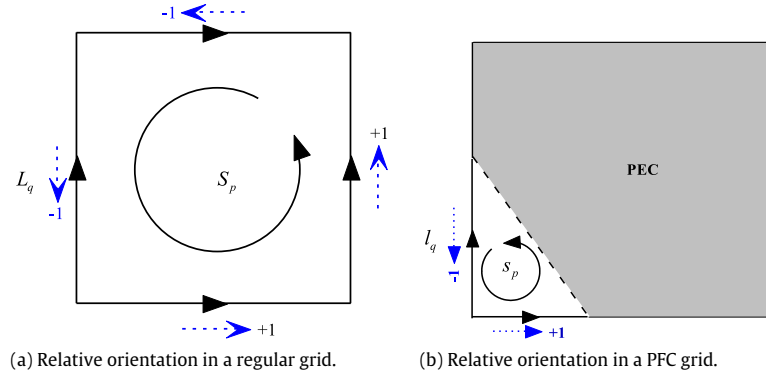(a) Relative orientation in a regular grid.   (b) Relative orientation in a PFC grid.

Fig. 2. The relative orientation between discrete faces and lines.

we correspondingly map x, y and z to 0, 1 and 2. If the value of u_0 is set as one of 0, 1 or 2, then the values of u_1 and u_2 can be given as

$$u_1 = (u_0 + 1) \bmod (3), \qquad u_2 = (u_0 + 2) \bmod (3) \tag{1}$$

where "mod" is the modulus operator.

In the grid system, (u, ijk) is defined as the multi-index of the grid elements. $l_{u,ijk}$ and $L_{u,ijk}$ are separately the non-PEC length and the total one of cell edge (i, j, k) along the direction u, defined as the natural orientation of $l_{u,ijk}$ and $L_{u,ijk}$. $s_{u,ijk}$ and $S_{u,ijk}$ are separately the non-PEC area and the total one of cell face (i, j, k) with the normal direction (natural orientation) u.

For convenience of definition, the direction of one edge element with a multi-index q is defined as $u_{q,0}$, and the direction of one facet with a multi-index p is defined as $\tilde{u}_{p,0}$. According to Eq. (1), we can get the direction $u_{q,1}$, $u_{q,2}$, $\tilde{u}_{q,1}$, and $\tilde{u}_{q,2}$.

Based on definition of the natural orientation of grid elements, the relative orientation between line and face can be decided. For a regular grid face S_p shown in Fig. 2(a), the line L_q is one of its boundary edges. If the natural orientation of L_q is reverse to the direction of the closed boundary orientation induced by natural orientation of S_p, we say that the orientation of L_q is relatively reverse to the orientation of S_p. On the contrary, we say that the orientation of L_q is relatively consistent with the orientation of S_p. The relative orientation relationship between L_q and S_p is noted as R_q^p. $R_q^p = -1$ means that L_q is relatively reverse to S_p, and $R_q^p = 1$ means that the orientation of L_q is consistent with the orientation of S_p. The definition manner of R_q^p is also suitable for PF faces shown in Fig. 2(b).

2.2. Review of symplectic FDTD and SC scheme

The dynamics of electromagnetic fields are described by Maxwell's equations, which in the differential form for a linear medium are

$$\varepsilon \frac{\partial}{\partial t} \boldsymbol{E} = \frac{1}{\mu} \nabla \times \boldsymbol{B} - \boldsymbol{J} \tag{2}$$

$$\frac{\partial}{\partial t} \boldsymbol{B} = -\nabla \times \boldsymbol{E} - \boldsymbol{M} \tag{3}$$

where $\boldsymbol{E}$ and $\boldsymbol{B}$ are the electric and magnetic fields, ε and μ are the permittivity and permeability of the medium, and $\boldsymbol{J}$ and $\boldsymbol{M}$ are the electric current density and magnetic current density.

According to the explicit symplectic partitioned Runge–Kutta (pRK) algorithm [20], the discrete forms of Eqs. (2) and (3) can be expressed as

$$\boldsymbol{B}^{n+(j+1)/r} = \boldsymbol{B}^{n+j/r} - b_j \Delta t \left(\nabla \times \boldsymbol{E}^{n+r} + \boldsymbol{M}^{n+j/r} \right) \tag{4}$$

$$\boldsymbol{E}^{n+(j+1)/r} = \boldsymbol{E}^{n+j/r} + \tilde{b}_j \Delta t \frac{1}{\varepsilon} \left(\frac{1}{\mu} \nabla \times \boldsymbol{B}^{n+(j+1)/r} - \boldsymbol{J}^{n+(j+1)/r} \right) \tag{5}$$
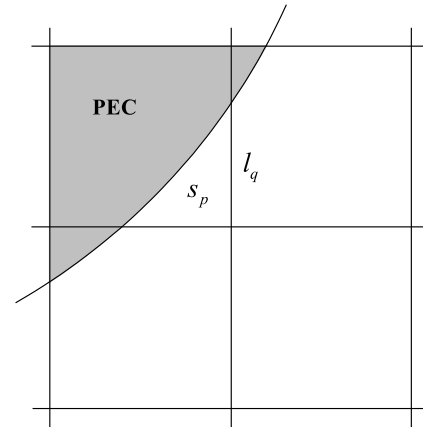

Fig. 3. A PF grid face.

where, $j = 0, \ldots, r-1$, b_j and $\tilde{b}_j$ are the coefficients for the explicit pRK algorithm, r is the order of the method, the values of b_j and $\tilde{b}_j$ can be selected referring to Ref. [20].

To introduce SC conformal method to pRK algorithm, the curl-operator in Eq. (4) needs to be expressed as an integral form. In context of FIT, the electromotive force along the oriented boundary of an arbitrary face S_p can be given as the following formula

$$V_p^n = \sum_{L_q \in \delta S_p} R_p^q \bar{l}_q L_q E_q^n \tag{6}$$

where $\bar{l}_{u,ijk} = l_{u,ijk}/L_{u,ijk}$.

For the small partially filled face shown in Fig. 3, the SC method is adopted to avoid reduction of the time step. That is to say, the value of $\bar{l}_{u_0,ijk}$ in Eq. (6) will be replaced in the following manner

$$\bar{l}_{u_0,ijk} = \min \left(2 \min \left(\bar{s}_{u_1,ijk}, \bar{s}_{u_1,ij(k-1)}, \bar{s}_{u_2,ijk}, \bar{s}_{u_2,i(j-1)k} \right), \bar{l}_{u_0,ijk} \right) \tag{7}$$

where $\bar{s}_{u,ijk} = s_{u,ijk}/S_{u,ijk}$.

Combining Eqs. (4)–(7), the conformal explicit symplectic pRK discrete equations can be obtained without reduction of time step.

2.3. Symplectic ADE-CFS-PML

Consider the Maxwell's equations in a lossless, source-free medium. Using complex stretched coordinates in the PML region, Faraday's and Ampere's laws in frequency domain are expressed as

$$-i\omega B_{u_0} = \frac{1}{s_{u_1}} \frac{\partial}{\partial x_{u_1}} E_{u_2} - \frac{1}{s_{u_2}} \frac{\partial}{\partial x_{u_2}} E_{u_1} \tag{8}$$

$$i\omega \varepsilon \mu E_{u_0} = \frac{1}{s_{u_1}} \frac{\partial}{\partial x_{u_1}} B_{u_2} - \frac{1}{s_{u_2}} \frac{\partial}{\partial x_{u_2}} B_{u_1} \tag{9}$$

where $s_v(v = u_0, u_1, u_2)$ are the stretched coordinate metric coefficients. Initially, these coefficients are chosen via the CFS-PML parameters,

$$s_v = \kappa_v + \frac{\sigma_v}{\alpha_v + i\omega\varepsilon_0} \quad (10)$$

where α_v, κ_v, and σ_v are the positive real functions with one variable x_v.

According to the construction manner of ADE-CFS-PML [28], the discrete form of Eq. (8) can be expressed as

$$B_{u_0}^{n+1/2} = B_{u_0}^{n-1/2} - \Delta t \left(\frac{1}{\kappa_{u_1}} \frac{\partial}{\partial x_{u_1}} E_{u_2}^n - \frac{1}{\kappa_{u_2}} \frac{\partial}{\partial x_{u_2}} E_{u_1}^n \right.$$
$$\left. + Q_{u_1,u_2}^{E^n} + Q_{u_2,u_1}^{E^n} \right) \quad (11)$$

$$Q_{u_1,u_2}^{E^n} = a_{u_1} Q_{u_1,u_2}^{E^{n-1}} + c_{u_1} \frac{\partial}{\partial x_{u_1}} E_{u_2}^{n-1} \quad (12)$$

$$Q_{u_2,u_1}^{E^n} = a_{u_2} Q_{u_2,u_1}^{E^{n-1}} - c_{u_2} \frac{\partial}{\partial u_2} E_{u_1}^{n-1} \quad (13)$$

$$a_{u_i} = \frac{\kappa_{u_i}\varepsilon_0}{\kappa_{u_i}\varepsilon_0 + \Delta t \left(\kappa_{u_i}\alpha_{u_i} + \sigma_{u_i} \right)}, \quad i = 1, 2 \quad (14)$$

$$c_{u_i} = \frac{\Delta t \sigma_{u_i}}{\kappa_{u_i} \left(\kappa_{u_i}\varepsilon_0 + \Delta t \left(\kappa_{u_i}\alpha_{u_i} + \sigma_{u_i} \right) \right)}, \quad i = 1, 2. \quad (15)$$

The discrete form of Eq. (9) can be obtained similarly.

For explicit symplectic pRK methods given by Eqs. (4) and (5), one time step is partitioned as multiple substeps, the scales of jth substep are given by parameters b_j and $\tilde{b}_j$. To partition Eqs. (11)–(15) using b_j, the explicit partitioned ADE-CFS-PML can be obtained corresponding to the symplectic pRK methods, and are expressed as

$$B_{u_0}^{n+(j+1)/r} = B_{u_0}^{n+j/r} - b_j\Delta t \left(\frac{1}{\kappa_{u_1}} \frac{\partial}{\partial x_{u_1}} E_{u_2}^{n+j/r} \right.$$
$$\left. - \frac{1}{\kappa_{u_2}} \frac{\partial}{\partial x_{u_2}} E_{u_1}^{n+j/r} + Q_{u_1,u_2}^{E^{n+j/r}} + Q_{u_2,u_1}^{E^{n+j/r}} \right) \quad (16)$$

$$Q_{u_1,u_2}^{E^{n+(j+1)/r}} = a_{j,u_1} Q_{u_1,u_2}^{E^{n+j/r}} + c_{j,u_1} \frac{\partial}{\partial x_{u_1}} E_{u_2}^{n+j/r} \quad (17)$$

$$Q_{u_2,u_1}^{E^{n+(j+1)/r}} = a_{j,u_2} Q_{u_2,u_1}^{E^{n+j/r}} - c_{j,u_2} \frac{\partial}{\partial x_{u_2}} E_{u_1}^{n+j/r} \quad (18)$$

$$a_{j,u_i} = \frac{\kappa_{u_i}\varepsilon_0}{\kappa_{u_i}\varepsilon_0 + b_j\Delta t \left(\kappa_{u_i}\alpha_{u_i} + \sigma_{u_i} \right)}, \quad i = 1, 2 \quad (19)$$

$$c_{j,u_i} = \frac{b_j\Delta t \sigma_{u_i}}{\kappa_{u_i} \left(\kappa_{u_i}\varepsilon_0 + b_j\Delta t \left(\kappa_{u_i}\alpha_{u_i} + \sigma_{u_i} \right) \right)}, \quad i = 1, 2 \quad (20)$$

where $j = 0, \ldots, r - 1$. The corresponding discrete equations for Ampere's laws are obtained similarly with the scaled steps by $\tilde{b}_j$.

$$-\frac{\Delta E_{u_1}^{n+j/r}}{\Delta x_{u_2}} \bigg|_{ijk} = \frac{V_{q,u_{q,1}}^{n+j/r}}{\Delta S_q},$$

$$V_{q,u_{q,1}}^{n+j/r} = \sum_{L_p \in \partial S_q} \left(r_p^q L_p E_p^{n+j/r} \frac{u_{p,0} - u_{q,1}}{u_{q,2} - u_{q,1}} \right) \quad (21)$$

$$\frac{\Delta E_{u_2}^{n+j/r}}{\Delta x_{u_1}} \bigg|_{ijk} = \frac{V_{q,u_{q,2}}^{n+j/r}}{\Delta S_q},$$

$$V_{q,u_{q,2}}^{n+j/r} = \sum_{L_p \in \partial S_p} \left(r_q^p L_p E_p^{n+j/r} \frac{u_p - u_{q,1}}{u_{q,2} - u_{q,1}} \right). \quad (22)$$

In Eq. (16), the difference operator cannot be directly converted to a finite integral formulation. Using the transforms (21) and (22),
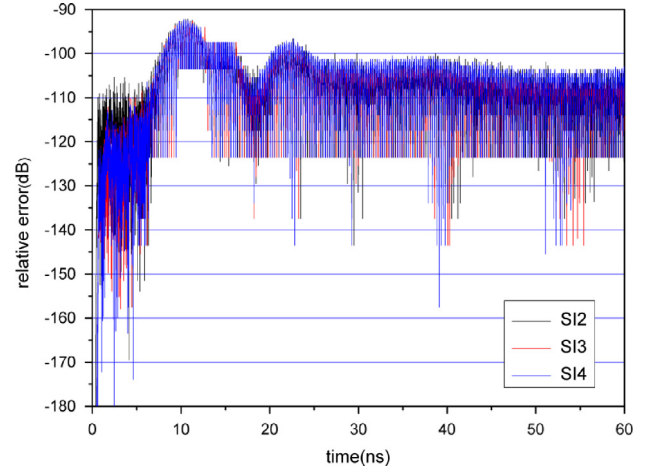

Fig. 4. Relative error versus time for the circular waveguide problem.

the difference operation in Eq. (16) can be transformed to the finite integral formulation, and then, the consistent formulation with FIT scheme can be obtained.

2.4. Conformal mode loading scheme

The types of HPM devices are identified into two classes: oscillators and amplifiers. During the simulation of these devices, the signals loading problem needs to be solved, including the injection of a voltage signal source and the launching of an input signal with one specified mode (not a TEM mode). That is to say, the mode patterns in the input port need to be solved.

For the injection of a voltage signal, the spatial distributions of potential in the port can be obtained by solving the following Laplace's equation

$$\nabla_T^2 \varphi = 0 \quad (23)$$

where ∇_T^2 is the transverse Laplacian operation excluding the normal direction of the port.

If the zero-order boundary conditions are set, using the second-order center-difference method, Eq. (23) can be expressed as the following discrete matrix equation,

$$\boldsymbol{a}\varphi = \boldsymbol{b}. \quad (24)$$

After the spatial distributions of potential are solved by using Eq. (24), the pattern of electric fields in the port can be computed.

For amplifiers or oscillators with phase controller for the purpose of coherent power combining, one signal with a specialized mode excluding the TEM mode needs to be injected from the input port. It is to say that the spatial distributions of the electric/magnetic fields with the specified mode in the port need to be computed first, which can be solved from the following two-dimensional wave equations,

$$\frac{1}{\varepsilon} \nabla_T \times \left(\frac{1}{\mu} \nabla_T \times \boldsymbol{E} \right) = -\frac{\partial^2 \boldsymbol{E}}{\partial t^2} \quad (25)$$

$$\frac{1}{\mu} \nabla_T \times \left(\frac{1}{\varepsilon} \nabla_T \times \boldsymbol{H} \right) = -\frac{\partial^2 \boldsymbol{H}}{\partial t^2} \quad (26)$$

where ∇_T is the transverse gradient operator excluding the normal direction of the port.

According to the FIT method, the discrete electric voltage $\widehat{e}_q$ and magnetic voltage $\widehat{h}_q$ are defined as

$$\widehat{e}_q = \int_{L_q} \boldsymbol{E} \cdot d\boldsymbol{l}, \quad \widehat{h}_q = \int_{\tilde{L}_q} \boldsymbol{H} \cdot d\boldsymbol{l} \quad (27)$$

where $\tilde{L}_q$ is the dual edge of the facet S_q.

Using the FIT method in the conformal grid system, Eqs. (25) and (26) are discretized as a matrix–vector form

$$A\,\hat{e} = -\frac{\mathrm{d}^2}{\mathrm{d}t^2}\,\hat{e} \tag{28}$$

$$\tilde{A}\,\hat{h} = -\frac{\mathrm{d}^2}{\mathrm{d}t^2}\,\hat{h} \tag{29}$$

where $\hat{e}$ and $\hat{h}$ are separately defined as the electric and magnetic voltage column vectors.

With a time-harmonic dependence $e^{i\omega t}$ for the fields, Eqs. (28) and (29) take the forms

$$A\,\hat{e} = \omega^2\,\hat{e} \tag{30}$$

$$\tilde{A}\,\hat{h} = \omega^2\,\hat{h}. \tag{31}$$

By solving the above equations, the distribution of the electric/magnetic fields in the port with eigenvalue ω^2 can be obtained.

After the distribution patterns of the electric/magnetic fields in the port are obtained with the desired time function, the input electric and magnetic fields are separately defined as $E_s(\mathbf{x}, t)$ and $H_s(\mathbf{x}, t)$. According to the surface equivalence theorem, the input electric/magnetic fields can be substituted as equivalent magnetic/electric current densities which are expressed as

$$J_{es} = -\hat{e}_n \times H_s \tag{32}$$

$$J_{ms} = \hat{e}_n \times E_s. \tag{33}$$

One specified mode can be loaded from the port by introducing the equivalent currents of the mode to discrete Maxwell's equations,

$$E^{n+1} = E^n + \frac{\Delta t}{\varepsilon}\nabla \times H^{n+1/2} - \frac{\Delta t}{\varepsilon}\left(J^{n+1/2} + J_{es}^{n+1/2}\right) \tag{34}$$

$$H^{n+3/2} = H^{n+1/2} - \frac{\Delta t}{\mu}\nabla \times E^{n+1} + \frac{\Delta t}{\mu}J_{ms}^{n+1/2}. \tag{35}$$

2.5. Conformal emission

A commonly used charge conserving weighting scheme is the linear weighting scheme, in which the charge weighting scheme can be expressed as

$$Q_{i_0 i_1 i_2} = \sum_\alpha q_\alpha \left(1 - w_{u_0}\right)\left(1 - w_{u_1}\right)\left(1 - w_{u_2}\right) \tag{36}$$

$$Q_{i_0+1 i_1 i_2} = \sum_\alpha q_\alpha w_{u_0}\left(1 - w_{u_1}\right)\left(1 - w_{u_2}\right),$$
$$i_0 i_1 i_2 = ijk,\ jki,\ kij \tag{37}$$

$$Q_{i_0 i_1+1 i_2+1} = \sum_\alpha q_\alpha \left(1 - w_{u_0}\right) w_{u_1} w_{u_2},$$
$$i_0 i_1 i_2 = ijk,\ jki,\ kij \tag{38}$$

$$Q_{i_0+1 i_1+1 i_2+1} = \sum_\alpha q_\alpha w_{u_0} w_{u_1} w_{u_2} \tag{39}$$

where i, j and k denote the indices of the Cartesian coordinates x, y and z. $w_{u_0} = \left(x_{u_0} - X_{ijk}\right)/\Delta x_{u_0}$, $\mathbf{x}$ refers to the position of the αth particle, and X_{ijk} is the position of the nearest lower mesh node.

The charge conserving currents generated in the cell can be expressed as

$$I_{u_0, i_0 i_1 i_2} = \sum_\alpha \frac{q_\alpha}{\Delta t}\Delta w_{u_0}\left(1 - \bar{w}_{u_1}\right)\left(1 - \bar{w}_{u_2}\right) \tag{40}$$

$$I_{u_0, i_0 i_1 i_2+1} = \sum_\alpha \frac{q_\alpha}{\Delta t}\Delta w_{u_0}\left(1 - \bar{w}_{u_1}\right)\bar{w}_{u_2} \tag{41}$$

$$I_{u_0, i_0 i_1+1 i_2} = \sum_\alpha \frac{q_\alpha}{\Delta t}\Delta w_{u_0}\bar{w}_{u_1}\left(1 - \bar{w}_{u_2}\right) \tag{42}$$

$$I_{u_0, i_0 i_1+1 i_2+1} = \sum_\alpha \frac{q_\alpha}{\Delta t}\Delta w_{u_0}\bar{w}_{u_1}\bar{w}_{u_2} \tag{43}$$

where $\Delta w = w^{n+1} - w^n$, and $\bar{w} = \left(w^{n+1} + w^n\right)/2$.

In the flow of PIC advancing scheme by using the above linear weighting algorithms, one particle is dropped into the cell without generating the self-consistent fields. After the particle has left the initial cell, the electric field is computed as if the charges with opposite sign remain in the first cell. However, Gauss's law is preserved in the next cell that the particle moves into. This implies that the key to charge conserving emission from perfectly conducting conformal boundaries is that the charge must initially be distributed completely inside PEC and does not weight any charges to the nodes inside the vacuum.

Similar to the cut-cell conformal emission algorithm [16], the cut-cell surface is triangulated to achieve a uniform emission density, and the initial emission position of emitted particle is located at the nearest PEC node to the conformal emission triangle. The difference is that the endpoint is decided by two components, the normal and transverse components. The former is the displacement under the normal electric field of the emission triangle within one time step; the latter is a random displacement parallel to the emission triangle, and its length is constrained by the shape of the emission triangle.

In one triangle, the point on it can be expressed as

$$\mathbf{p} = u\mathbf{P}_0 + v\mathbf{P}_1 + w\mathbf{P}_2,$$
$$u > 0,\quad v > 0,\quad w > 0,\ \text{and } u + v + w = 1 \tag{44}$$

where $\mathbf{P}_0$, $\mathbf{P}_1$, and $\mathbf{P}_2$ are the vertices of the triangle, u, v, and w are the barycentric coordinates. If u and v are the random values in interval $(0, 0.5)$, and $w = 1 - u - v$, then the random transverse component can be selected as the following expression

$$d\mathbf{x}_T = \mathbf{p} - \mathbf{O} \tag{45}$$

where $\mathbf{O}$ is the barycenter of the triangle.

3. Numerical examples

In this section, numerical examples are separately given to test the symplectic ADE-CFS-PML, conformal mode loading, and conformal emission algorithms. Finally, a magnetically insulated line oscillator (MILO) is simulated to test the SC Symplectic PIC code presented in this paper.

3.1. Numerical examples for symplectic ADE-CFS-PML

The symplectic ADE-CFS-PML formulation is validated via calculating the electromagnetic wave propagating in a circular waveguide, whose radius and height are 55.0 and 120.0 mm. The waveguide is padded with additional ten cells of PML on two ends. The spatial step is 5.0 mm in all three directions. The origin point of the discrete space domain is set at the center of the model. The electric field along z-axis is probed at the point (12.5, 12.5, 35.0 mm). The simulation time is 60.0 ns. The time step is set as

$$\Delta t = 0.95 \times \frac{1}{c\sqrt{1/\left(\Delta x\right)^2 + 1/\left(\Delta y\right)^2 + 1/\left(\Delta z\right)^2}} \tag{46}$$

where c is the speed of light.

The excitation source is chosen as a dipole with the form of sine-modulated Gaussian pulse, it occupies one grid step length at $(-12.5, -12.5, -40.0$ mm) along z axis,

$$J_z = \cos\left(2\pi f\right)e^{-4\pi(t-t_0)^2/\tau^2} \tag{47}$$

(a) TE_{11}. (b) TE_{21}. (c) TE_{01}.
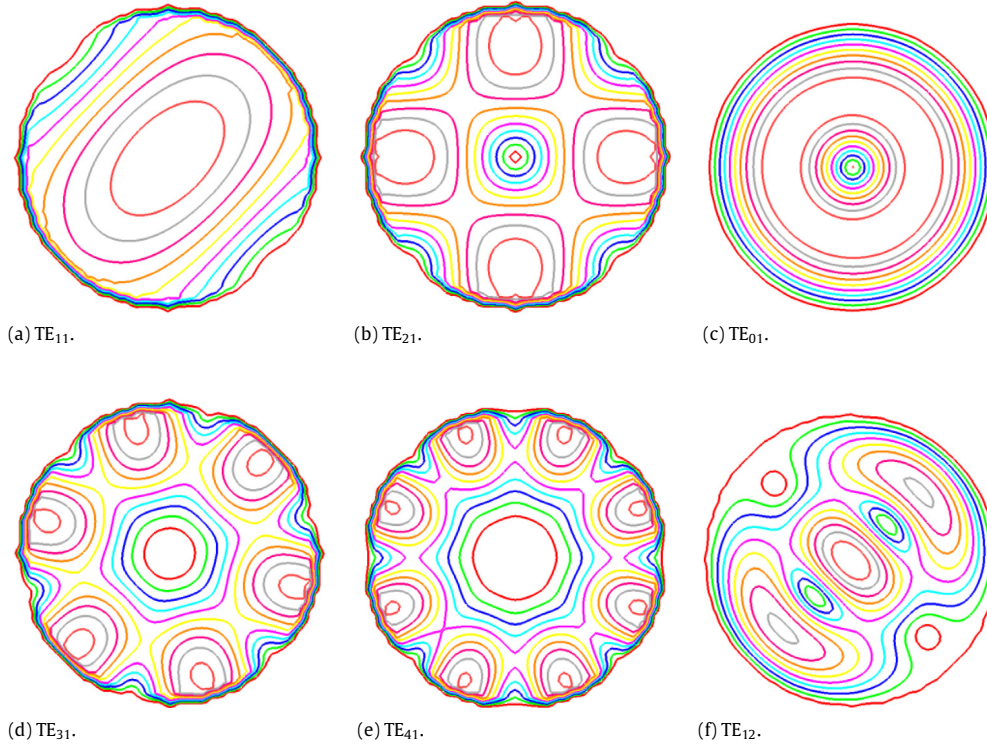
(d) TE_{31}. (e) TE_{41}. (f) TE_{12}.

Fig. 5. Some TE mode patterns of a circular waveguide.

Table 1
Cutoff frequencies of TE modes of a circular waveguide.

Mode	TE_{11}	TE_{21}	TE_{01}	TE_{31}	TE_{41}	TE_{12}
Analytical Freq (GHz)	1.598	2.651	3.327	3.647	4.616	4.628
Numerical Freq (GHz)	1.598	2.649	3.326	3.643	4.614	4.625

where J_z is the current density along z axis, f is the modulation frequency, τ is the pulse duration, t_0 is the peak time of the pulse. In the simulation, we choose $f = 2.0$ GHz, $\tau = 20/f$, and $t_0 = 20/f$.

To study the reflection error due to the symplectic ADE-CFS-PML, a reference problem is also simulated. The two ends of the waveguide are extended sufficiently long so that no reflection from the exterior boundary would occur during the simulation. The relative error is defined as

$$\text{Error}_{dB} = 20 \log_{10} \frac{\left| E_z(t) - E_z^{\text{ref}}(t) \right|}{\max \left\{ \left| E_z^{\text{ref}}(t) \right| \right\}} \quad (48)$$

where E_z represents the field computed using the original problem, E_z^{ref} represents the field computed using the reference problem, "max" represents the maximum value over all time.

In our simulation, the constitutive parameters of symplectic ADE-CFS-PML σ, κ, and α are set with the same manner as in [33]. Both σ and κ are scaled with third-order polynomial scaling ($m = 3$), with $\kappa_{\max} = 40.0$, $\sigma_{\text{ratio}} = 7.5$, and $\alpha_{\max} = 0.0$. The results are shown in Fig. 4 with different orders of symplectic integrator. The results show that the truncation error of symplectic ADE-CFS-PML could be less than −90 dB.

3.2. Numerical examples for conformal mode loading

The numerical model is selected the same as that used in Section 3.1. For the circular waveguide, the cutoff frequency of a TE mode is given by

$$f_{CTE_{mn}} = \frac{x_{mn}}{2\pi a \sqrt{\mu \varepsilon}} \quad (49)$$
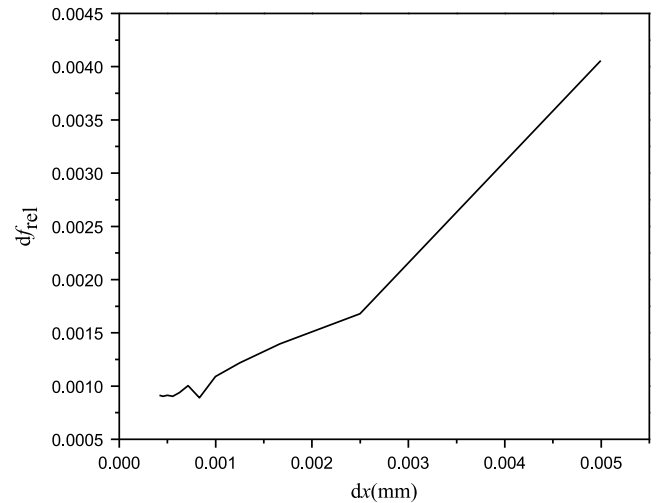
Fig. 6. Df_{rel} versus dx for the TE_{01} mode in the circular waveguide.

where x_{mn} is the mth root of the function $J_n'(x)$, which is the derivative of Bessel function of the first kind.

Some cutoff frequencies and mode patterns of TE modes for the test model are numerically computed by using Eq. (30), and the results are separately shown in Table 1 and Fig. 5. The numerical values are compared with the analytical ones, the errors could be as low as 0.1%.

To observe the effect of the grid size on the numerical accuracy, we define the relative difference of the cutoff frequencies between
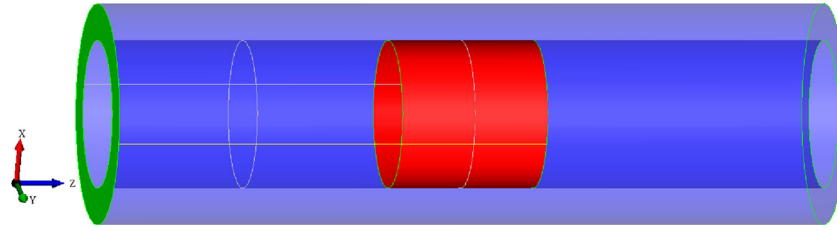
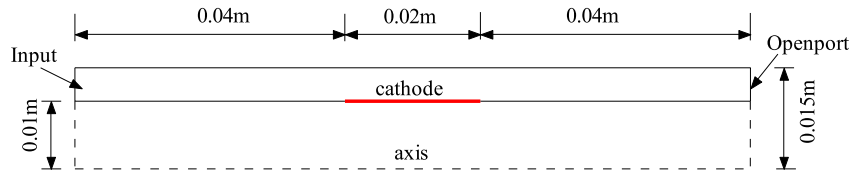**Fig. 7.** Schematic view of the coaxial cylindrical diode.

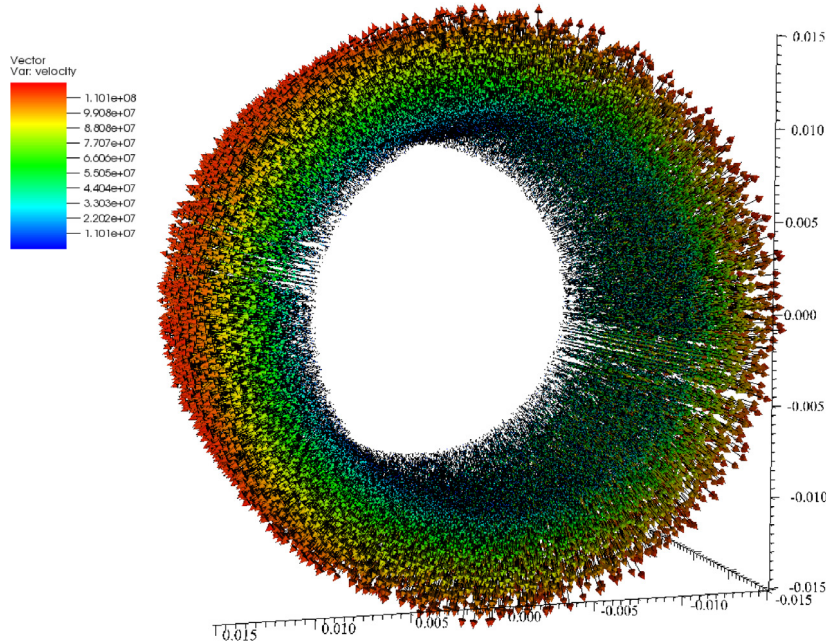**Fig. 8.** The dimensions of the coaxial cylindrical diode.

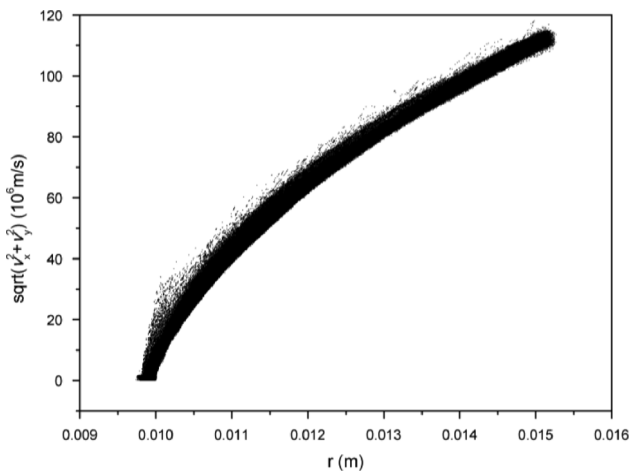

Fig. 9. Velocity space of particles at 14.1 ns.

Fig. 10. Phase-space of radial velocity of electron for coaxial emission at 14.1 ns.

the numerical and analytic results as

$$\mathrm{d}f_{\mathrm{rel}} = \frac{|f_{\mathrm{num}} - f_{\mathrm{ana}}|}{f_{\mathrm{ana}}}. \tag{50}$$

We calculate the relative difference of the cutoff frequency for the TE_{01} mode in the circular waveguide, and present it versus the grid size dx in Fig. 6. It can be seen from this figure that the relative difference between the numerical and analytic results decreases basically with reduction of the grid size.

3.3. Numerical examples for conformal emission

A coaxial cylindrical diode is chosen to test the conformal emission algorithm, which is schematically shown in Fig. 7, and its dimensions are shown in Fig. 8. The anode radius is 15.0 mm and the cathode radius is 10.0 mm that gives an A–K gap of 5.0 mm. The input A–K gap voltage is 50.0 kV, and its rise time is 1.0 ns. The spatial step is 0.2 mm in all three directions. The
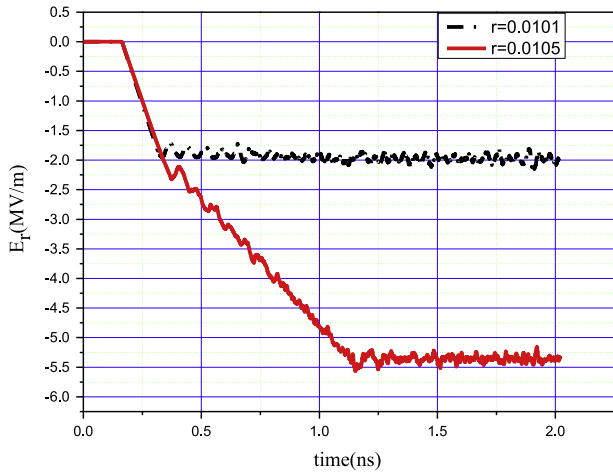
Fig. 11. Instantaneous radial electric field near the cathode surface.

particles are emitted according to the charge conservation method. Fig. 9 shows the velocity space distributions of particles inside the coaxial cylindrical diode, and Fig. 10 shows the phase-space of radial velocity of particle along the radial gap between the coaxial cylinders.

The results show that the beam produced by using conformal charge emission method expands due to the space charge, which is a fairly parabolic profile as expected.

The radial component E_r on the cathode surface remains zero as a function of time due to the explosive emission of electrons. Nevertheless, E_r is not zero at the half index of the grid near the cathode surface to maintain the explosive emission of electrons [1]. Fig. 11 shows E_r at the first and third half indices of the grid near

the cathode surface. It can be seen that they grow at first and then remain nearly unchanged as a function of time.

3.4. Numerical example for the simulation of HPM devices

The MILO is a low-impedance cross-field microwave device, in which the electrons are emitted from a cylindrical cathode, and it is chosen as the numerical example for testing the conformal algorithms introduced in this paper.

Fig. 12 shows the dimensions of MILO geometry, and its 3D computational model is shown in Fig. 13. Figs. 14 and 15 show respectively the conformal grids of three cross sections of the device and the triangular mesh of the cathode. Fig. 16 gives the details of the conformal grids. This device is driven by a voltage of 2.1 MV with the rise time of 1 ns. The whole computational region is discretized into $182 \times 182 \times 587$ ($n_x \times n_y \times n_z$) cells, and the time step is 6.556×10^{-4} ns. Numerical simulations are conducted on this device with the second and third symplectic integrators.

Typical results are shown in Figs. 17–22. Fig. 17 shows the velocity space of particles at 13.7688 ns. Fig. 18 represents the input voltage. Fig. 19 shows the time history of the electric fields at the test point (0.0, 32.0, 230.0 mm), and Figs. 20 and 21 give the spectrum of output signal. From Figs. 19 and 20, the amplitude of E_z computed with the third SI method is smaller than one computed with the second SI method. With the FFT analysis, the excited high frequencies with the third SI method are less than the second SI method, and to some extent the high frequency numerical Cherenkov radiation is restrained with the third SI method. Fig. 22 gives the output microwave power generated in the MILO device. Additionally, comparing Fig. 22(a) and (b), the output microwave power computed with the third SI method is smoother.

For the sake of comparison, numerical results are also provided by using the 2.5D UNIPIC code for the same MILO device [12].
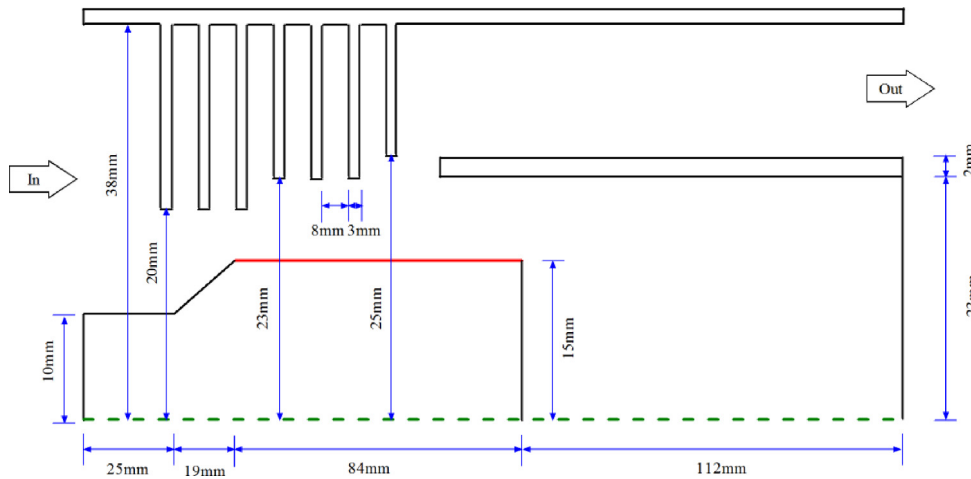

Fig. 12. MILO geometry. The red line is the cathode, the dashed green line is the axis. (For interpretation of the references to color in this figure legend, the reader is referred to the web version of this article.)
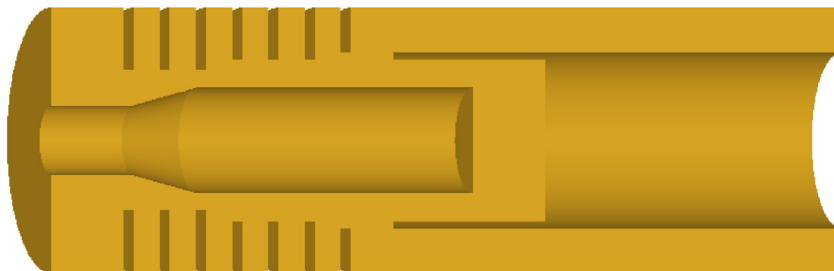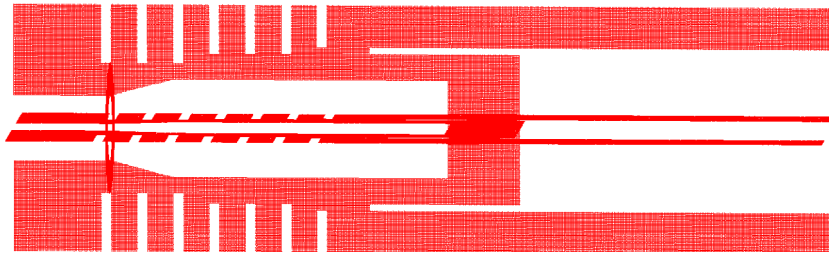

Fig. 13. 3D model of MILO.

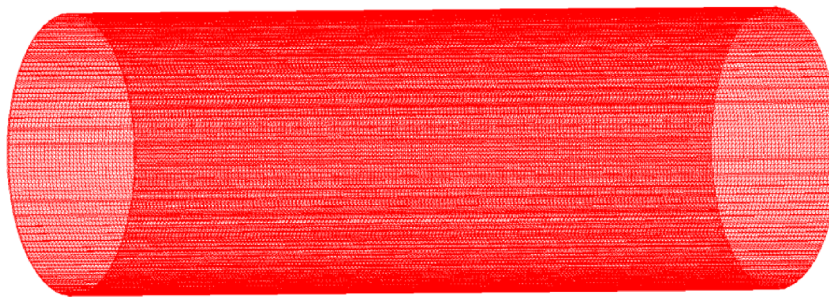**Fig. 14.** Conformal grids of three different sections of MILO.

Fig. 15. The triangular mesh of the MILO's cathode.

(a) The details of one section.

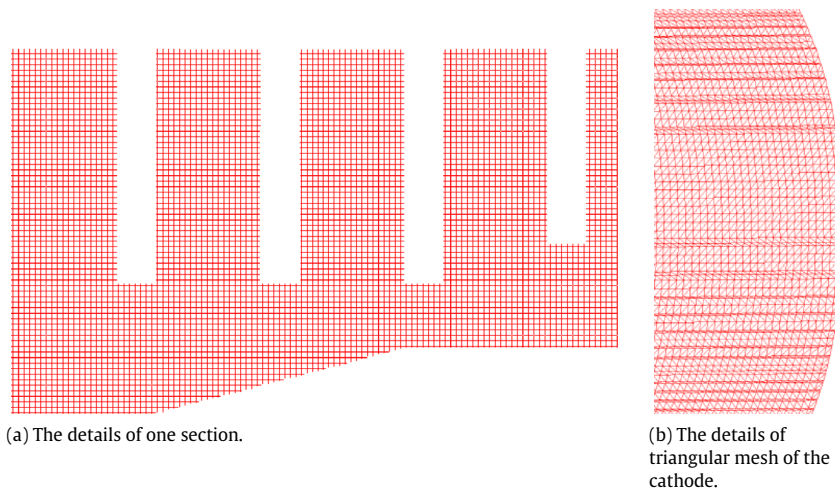(b) The details of triangular mesh of the cathode.

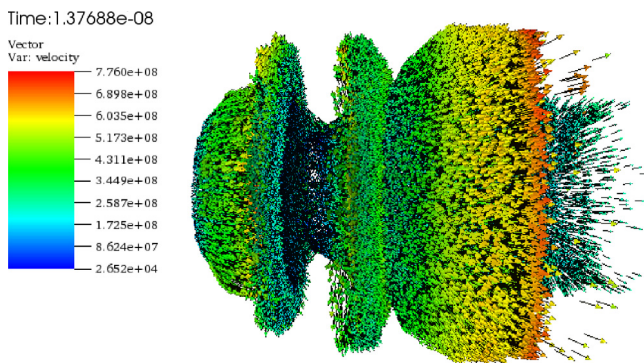**Fig. 16.** The details of the conformal grids.

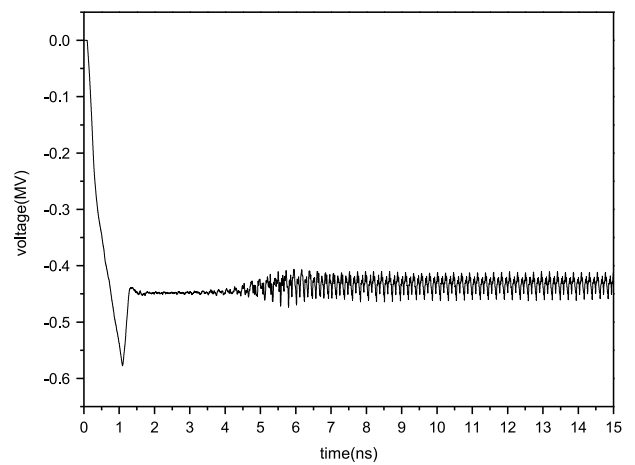**Fig. 17.** Velocity space of particles inside MILO with the third SI method.

Fig. 18. Input voltage of MILO recorded when using the third symplectic integrator.

Fig. 23 is the 2D computational model of MILO discretized into $480 \times 76 \, (n_z \times n_r)$ cells. Figs. 24–26 respectively represent the input voltage, the spectrum of output signal, and the output microwave power. It can be seen that the results calculated by using these two codes agree well.

Next, we discuss the computational expenses cost by the new code and the UNIPIC code. First, the UNIPIC code is a
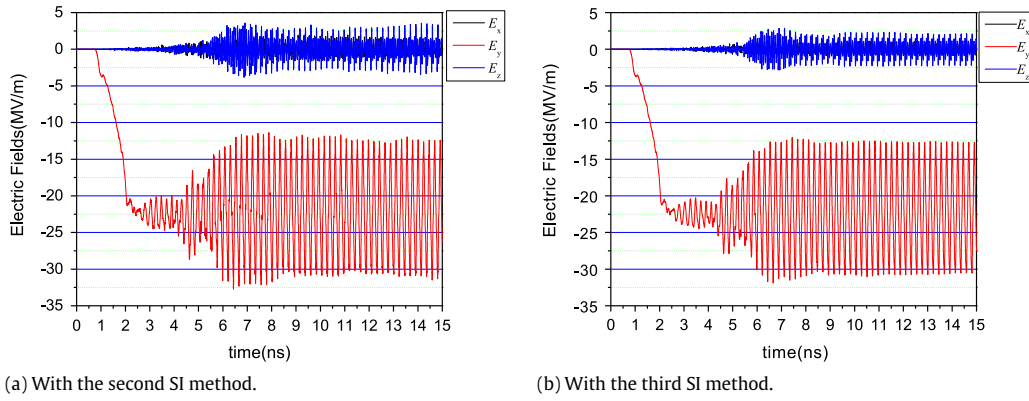
(a) With the second SI method.

(b) With the third SI method.

Fig. 19. The electric fields at the test point (0.0, 32.0, 230.0 mm).

(a) With the second SI method.
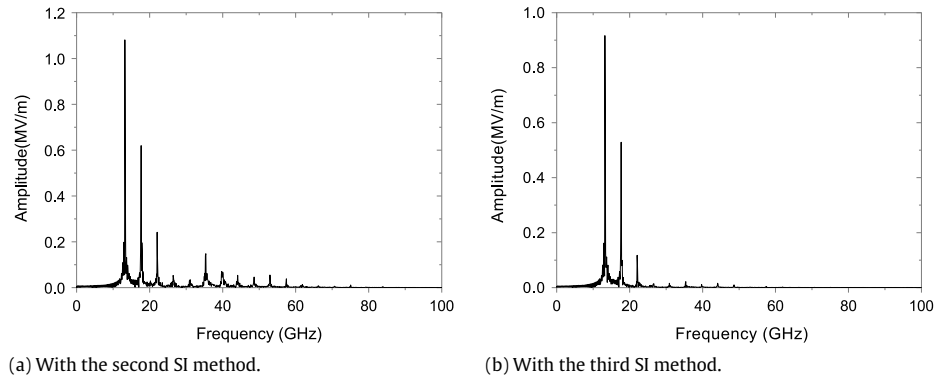
(b) With the third SI method.

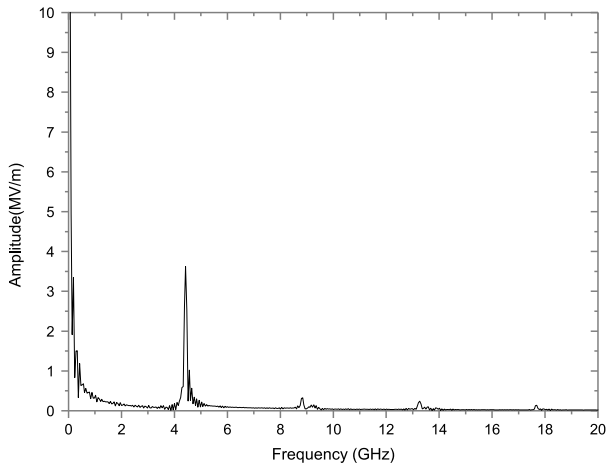**Fig. 20.** FFT from 7 to 15 ns of E_z.

Fig. 21. FFT of E_y computed with the third SI method.

two-and-a-half dimensional one, which solves the six components of electromagnetic field (E_r, E_ϕ, E_z, H_r, H_ϕ, and H_z) and five physical quantities of particle (v_r, v_ϕ, v_z, x_r, and x_z). Second, this new 3D SC symplectic PIC method should solve the six components of electromagnetic field (E_x, E_y, E_z, H_x, H_y, and H_z) and six physical quantities of particle (v_x, v_y, v_z, X_x, X_y, and X_z), meanwhile, it needs also to deal with the conformal boundary. Therefore, for the same numbers of particles to be tracked, the computational cost per cell of the 3D SC symplectic PIC method is a little bit bigger than that of the UNIPIC code. This is the case for the second order SI method, whose computational cost is nearly one third of that for the third order SI method.

The above studied MILO is a typical device with a cylindrical cathode surface which needs the conformal emission algorithm,

and it can also be simulated by using the 2.5D PIC code. But some HPM devices can be simulated only by using 3D PIC code, for example, the power combiner composed of two or more single HPM tubes. Recently, Xiao et al. studied the power combination of two phase-locked relativistic backward wave oscillators (RBWO) numerically and experimentally [36]. The computational model of this power combiner is shown in Fig. 27. Due to the complicated slow wave structure of the klystron-like RBWO and intersection of the two RBWOs, it is very difficult to get correct physical picture of the power summation from the two RBWOs by using the UNIPIC-3D code with staircase meshes. And hence, Xiao et al. designed and investigated this kind of power combiner at the X band by using our new 3D SC symplectic PIC code [36]. The conformal meshes constructing the power combiner are also shown in Fig. 27. By the PIC simulation, the output power, summation efficiency, and distributions of electromagnetic field inside the combiner were provided. The numerical results agreed well with the experimental ones [36].

To suppress the high frequency waves, the damping scheme is usually adopted in the particle simulations. In this paper, Friedman damping scheme is employed [29]. The range of damping factor can be set as [0, 0.5], but it is usually [0.1, 0.4]. In our simulation of the MILO, the damping factor is taken as 0.3.

4. Conclusion

This paper presents a 3D SC symplectic PIC method for simulations of high power microwave devices. Comparing with the traditional EM-PIC method, the symplectic integrator is employed to update the fields in time domain, and the SC scheme is used to solve the fields around the curved boundaries. Accordingly, the symplectic formulas of ADE-CFS-PML are given for truncating the open ports, numerical results show that the maximum relative
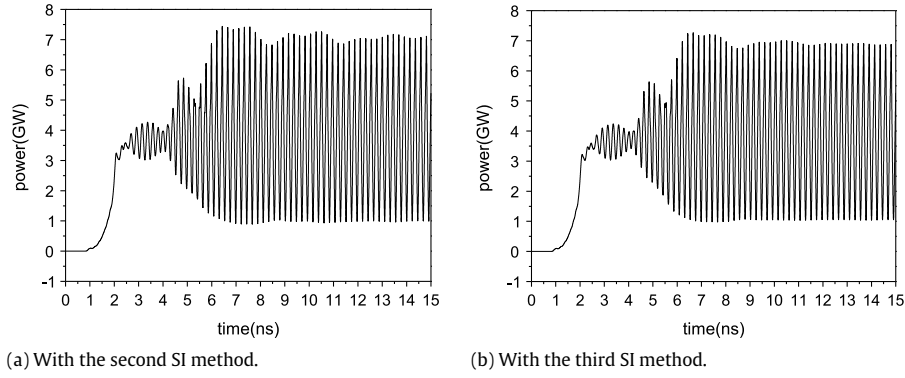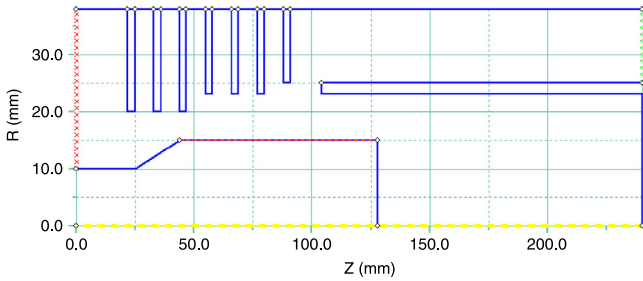
(a) With the second SI method.

(b) With the third SI method.

Fig. 22. Output microwave power of MILO.

Fig. 23. 2D model of MILO for UNIPIC.

Fig. 24. Input voltage of MILO in UNIPIC.

Fig. 25. Spectrum of electric field generated in MILO obtained by UNIPIC.
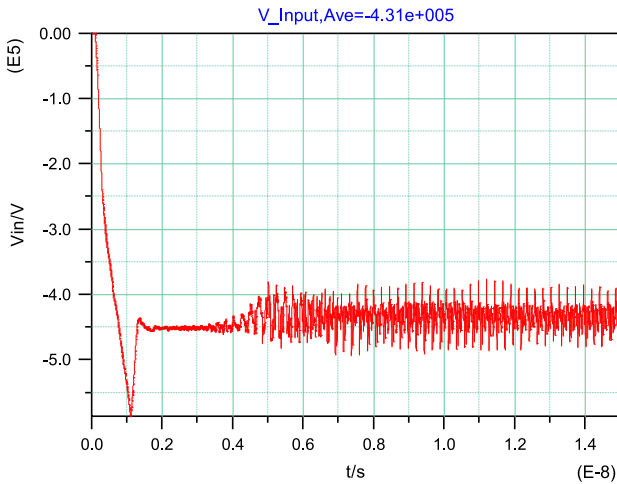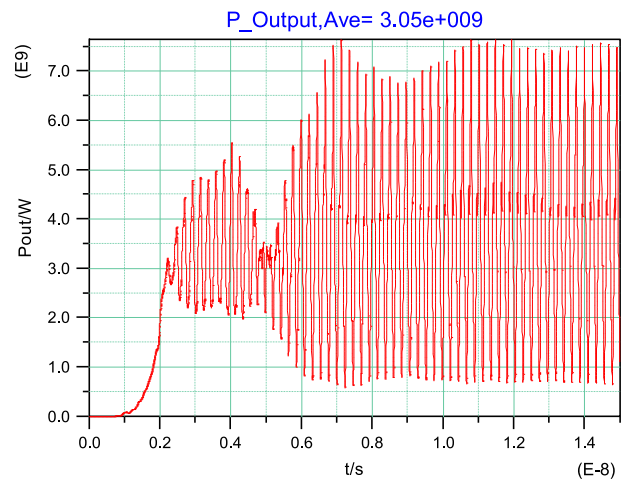

Fig. 26. Output microwave power of MILO obtained by UNIPIC.

error is less than 90 dB. For conformal signals injection, the computing algorithms of the TEM, TE, and TM mode patterns are given for the waveguide ports, and these patterns are loaded as the input signals according to the surface equivalence theorem. Numerical results show that the algorithms can give the right mode patterns and the errors of cutoff frequencies could be as low as 0.1%. The modified cut-cell conformal emission is also given, and a coaxial cylindrical diode is chosen to test the algorithm. Numerical results show that the beam produced by using the conformal charge emission method expands as a parabolic profile as expected. Finally, to verify the conformal algorithms, a MILO is simulated, and the results are compared to the numerical results provided by using the 2.5D UNIPIC code, which show that they agree well. The results also show that the high order SI method can restrain the numerical Cherenkov radiation.

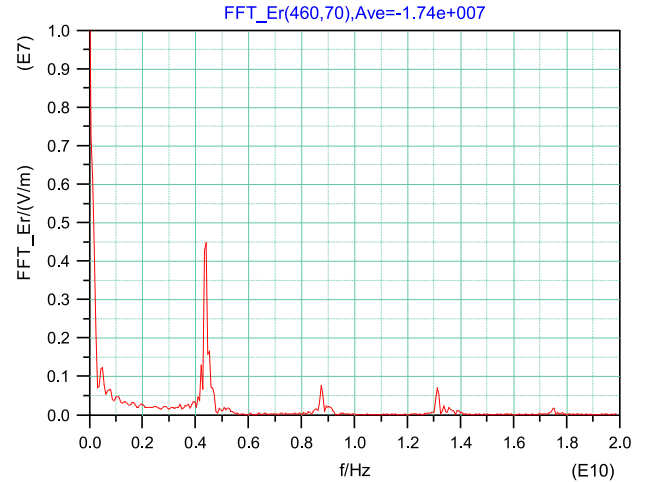For conformal emission of the particles, the perfect charge conservation emission scheme perhaps may be given by combining the weighting scheme on unstructured grids and on structured grids [37] in the hybrid FVTD/FDTD frameworks recommended in Ref. [38].
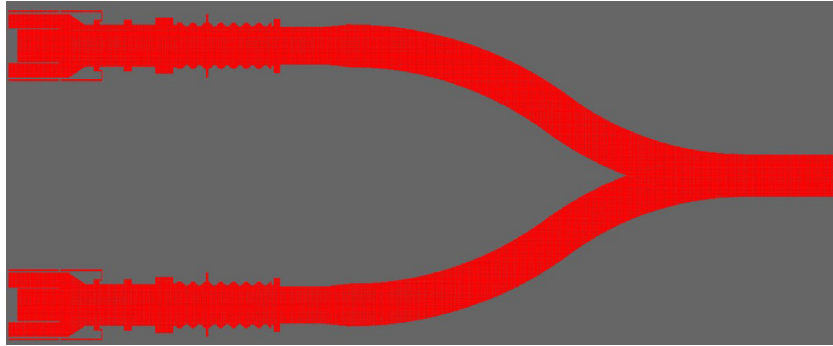
Acknowledgments

Fig. 27. The numerical model of the power combiner.

References

[1] R.J. Barker, E. Schamiloglu, High-Power Microwave Sources and Technologies, IEEE Press, New York, 2001.
[2] C.K. Birdsall, A.B. Langdon, Plasma Physics via Computer Simulation, McGraw-Hill, New York, 1985.
[3] K.S. Yee, IEEE Trans. Antennas and Propagation 14 (1966) 302–307.
[4] T. Weiland, Electron. Commun. AEU 31 (1977) 116–120.
[5] T. Weiland, Int. J. Numer. Model. 9 (1996) 295–319.
[6] B. Goplen, L. Ludeking, D. Smith, G. Warren, Comput. Phys. Comm. 87 (1995) 54–86.
[7] J.P. Verboncoeur, A.B. Langdon, N.T. Gladd, Comput. Phys. Comm. 87 (1995) 199–211.
[8] V.P. Tarakanov, User's Manual for Code KARAT, Berkeley Research Associates, Springfield, 1992.
[9] J.J. Havranek, B.J. Smith, A portable parallel particle in cell code, AIAA #96-0835, in: 34th Aerospace Sciences Meeting, Reno, NV, January 15–18, 1996. http://dx.doi.org/10.2514/6.1996-835.
[10] M. Clemens, S. Drobny, H. Kruger, P. Pinder, O. Podebrad, B. Schillinger, B. Trapp, T. Weiland, M. Wilke, M. Bartsch, U. Becker, M. Zhang, The electromagnetic simulation software package MAFIA 4, in: ICCEA'99. 1999, pp. 565–568. http://dx.doi.org/10.1109/ICCEA.1999.825246.
[11] C. Nieter, J.R. Cary, J. Comput. Phys. 196 (2004) 448–473.
[12] J. Wang, D. Zhang, C. Liu, Y. Li, Y. Wang, H. Wang, H. Qiao, X. Li, Phys. Plasmas 16 (2009) 033108.
[13] J. Wang, Z. Chen, Y. Wang, D. Zhang, C. Liu, Y. Li, H. Wang, H. Qiao, M. Fu, Y. Yuan, Phys. Plasmas 17 (2010) 073107.
[14] L. Pebernet, X. Ferrieres, V. Mouysset, F. Rogier, Pierre Degond, A discontinuous Galerkin formalism to solve the Maxwell–Vlasov equations. Application to high power microwave sources, in: Scientific Computing in Electrical Engineering, SCEE 2010, in: The Series Mathematics in Industry, vol. 16, Springer-Verlag, Berlin, Heidelberg, 2012, pp. 183–192.
[15] T.G. Jurgens, A. Taflove, K. Umashankar, T.G. Moore, IEEE Trans. Antennas and Propagation 40 (1992) 357–366.
[16] D. Smithe, P. Stoltz, J. Loverich, C. Nieter, S. Veitzer, Development and application of particle emission algorithms from cut-cell boundaries in the vorpal EM-FDTD-PIC simulation tool, in: IEEE Vacuum Electronics Conference, 2008, pp. 217–218.
[17] X. Tian, Q.H. Liu, IEEE Microw. Wirel. Compon. Lett. 14 (2004) 551–553.
[18] I.A. Zagorodnov, R. Schuhmann, T. Weiland, J. Comput. Phys. 225 (2007) 1493–1507.
[19] J. Chen, J. Wang, IEEE Trans. Antennas and Propagation 55 (2007) 3613–3619.
[20] J.M. McMahon, S.K. Gray, G.C. Schatz, J. Comput. Phys. 228 (2009) 3421–3432.
[21] B.B. Godfrey, J. Comput. Phys. 15 (1974) 504–521.
[22] B.B. Godfrey, J. Vay, J. Comput. Phys. 267 (2014) 1–6.
[23] B.B. Godfrey, Review and recent advances in pic modeling of relativistic beams and plasmas, in: Proceeding of 2014 Advanced Accelerator Concepts Workshop, 2014.
[24] B.B. Godfrey, J. Vay, Improved numerical Cherenkov instability suppression in the generalized PSTD PIC algorithm, 2015. arXiv Preprint arXiv:1502.01387.
[25] J. Xiao, J. Liu, H. Qin, Z. Yu, Phys. Plasmas 20 (2013) 102517.
[26] J. Xiao, J. Liu, H. Qin, Z. Yu, N. Xiang, Phys. Plasmas 22 (2015) 092305.
[27] F.L. Teixeira, W.C. Chew, Int. J. Numer. Model. 13 (2000) 441–455.
[28] S.D. Gedney, B. Zhao, IEEE Trans. Antennas and Propagation 58 (2010) 838–847.
[29] A. Friedman, J.J. Ambrosiano, J.K. Boyd, S.T. Brandon, D.E. Nielden, P.W. Rambo, Damped time advance methods for particles and EM fields, in: US-Japan Workshop on Advanced Computer Simulation Technique Applied to Plasmas and Fusion, 1990.
[30] Y. Wang, M. Fu, Z. Chen, L. Cai, H. Xie, J. Wang, High Power Laser Part. Beams 23 (2011) 2994–2998.
[31] J.A. Roden, S.D. Gedney, Microw. Opt. Technol. Lett. 27 (2000) 334–339.
[32] J. Wang, Y. Wang, D. Zhang, IEEE Trans. Plasma Sci. 34 (2006) 681–690.
[33] Y. Wang, J.G. Wang, Z.G. Chen, Chin. Phys. B 24 (2015) 024101.
[34] T.Zh. Esirkepov, Comput. Phys. Comm. 135 (2001) 144–153.
[35] http://www.opencascade.org [EB/OL].
[36] R. Xiao, Y. Deng, Y. Wang, Z. Song, J. Li, J. Sun, C. Chen, Appl. Phys. Lett. 107 (2015) 133502.
[37] H. Moon, F.L. Teixeira, Y.A. Omelchenko, Comput. Phys. Comm. 194 (2015) 43–53.
[38] C.S. Meierbachtol, A.D. Greenwood, J.P. Verboncoeur, B. Shanker, IEEE Trans. Plasma Sci. 43 (2015) 3778–3793.